Journal of Alloys and Compounds 741 (2018) 368–376

Contents lists available at ScienceDirect

Journal of Alloys and Compounds

journal homepage: http://www.elsevier.com/locate/jalcom

Sulfur codoping enables efficient oxygen electroreduction on FeCo alloy encapsulated in N-Doped carbon nanotubes

Dengke Zhao [a], Ligui Li [a, b, *], Lihong Xie [a], Ni Zhou [a], Shaowei Chen [a, c]

[a] Guangzhou Key Laboratory for Surface Chemistry of Energy Materials, New Energy Research Institute, School of Environment and Energy, South China University of Technology, Guangzhou Higher Education Mega Center, Guangzhou, 510006, China
[b] Guangdong Provincial Key Laboratory of Atmospheric Environment and Pollution Control, School of Environment and Energy, South China University of Technology, Guangzhou, 510006, China
[c] Department of Chemistry and Biochemistry, University of California, 1156 High Street, Santa Cruz, CA, 95064, USA

ARTICLE INFO

Article history:
Received 24 April 2017
Received in revised form
18 December 2017
Accepted 10 January 2018
Available online 11 January 2018

Keywords:
Oxygen reduction reaction
Iron-cobalt alloy
Carbon nanotube
Sulfur doping
Charge transfer

ABSTRACT

Sulfur- and nitrogen-codoped peapod-like carbon nanotubes are facilely prepared via pyrolyzing Fe- and Co-containing Prussian blue analogues supported on trithiocyanuric acid. Combined studies with X-ray diffraction, X-ray photoelectron spectroscopy and high-resolution transmission electron microscopy measurements reveal the encapsulation of metallic FeCo alloy in such carbon nanotubes with a wall thickness of ca. 2.60 nm. Electrochemical measurements show that sulfur codoping with nitrogen dramatically enhances the catalytic activity towards oxygen reduction reaction compared with that of FeCo alloy encapsulated in N-doped only carbon nanotubes, and the sample prepared at a pyrolysis temperature of 800 °C is the best one among the series, exhibiting a more positive half-wave potential of +0.838 V, nearly 100% enhancement in kinetic current, a higher operation stability and stronger immunity to the negative impacts of fuel crossover than commercial Pt/C catalysts. The remarkable improvement of catalytic activity is ascribed to the intensified charge transfer from encapsulated FeCo alloy nanoparticles to thin walls of CNTs upon the additional sulfur doping besides nitrogen. The present results highlight the importance of deliberate doping and structuring in the development of more efficient catalysts based on metal nanoparticles encapsulated in CNTs for high-performance electrochemical energy devices.

1. Introduction

Proton-exchange membrane fuel cell (PEMFC) and metal-air batteries, which integrate a high energy density and remarkable power conversion efficiency, represent two promising eco-friendly electrochemical energy technologies to mitigate/solve the nowaday energy crisis and sever environmental problems [1]. Oxygen reduction reaction (ORR) is a key half-cell reaction at the cathodes of these two green technologies [2,3]. Yet, due to its complicated reaction process and sluggish charge-transfer kinetics, ORR largely determines the performance of these two families of devices. Therefore, effective catalysts are required to induce the cathodic ORR along the preferred reaction pathway and concurrently accelerate the reaction rate. Nevertheless, the choice of efficient ORR catalyst has remained rather limited, normally the noble metal nanoparticles of Pt, Pd and their alloys with nonprecious transition metals [4–6]. However, the noble-metal based catalysts encounter many critical challenges in practical applications, including expensiveness, scarcity, weak immunity to CO poisoning, low tolerance to fuel-crossover effect and dissolution/aggregation in electrolyte solution, which heavily hinder their commercial use in PEMFC and metal-air batteries [7–9]. Therefore, development of low-cost high-performance catalysts using earth-abundant elements has been deemed as a judicious way to break through the current predicament.

Recently, intensive research efforts in exploration of ORR electrocatalysts have been devoting to nonprecious transition metal (Fe, Co etc.) and heteroatom (N, S, B, P, Se, etc.) co-doped carbons [10] such as carbon nanotubes [11–14], graphene [9,15,16] and active carbons [17–19]. The high performance-price ratio of these

* Corresponding author. Guangzhou Key Laboratory for Surface Chemistry of Energy Materials, New Energy Research Institute, School of Environment and Energy, South China University of Technology, Guangzhou Higher Education Mega Center, Guangzhou, 510006, China.
E-mail address: esguili@scut.edu.cn (L. Li).

https://doi.org/10.1016/j.jallcom.2018.01.144
0925-8388/

carbon catalysts makes them a class of high potential alternatives to Pt-based catalysts. Of these, nonprecious transition metal nanoparticles encapsulated in carbon materials represent an emerging type of versatile carbon composites which show apparent catalytic activities in hydrogen evolution reaction (HER) [20,21], oxygen evolution reaction (OER) [22,23] and oxygen reduction reaction (ORR) [8,24–26]. For example, Asefa's group [21] found that cobalt nanoparticles encapsulated in N-doped CNTs could effectively catalyze HER at a wide range of pH. Bao's group [27,28] reported the observation of highly active electroreduction of oxygen on peapod-like N-doped CNTs embedding FeCo alloy nanoparticles, and they elucidated that the high ORR activity of such composites was mainly derived from the electron interaction between embedded FeCo nanoparticles and thin walls of N-doped carbon nanotubes. Similarly, efficient bifunctional electrocatalysts for ORR and OER were observed by Chen's group [25,29] on a strongly coupled 3D N-doped porous carbon nanosheet hybrid with CoNi Alloy encapsulated in N-doped CNTs. These pioneer works suggest that encapsulating metal or metal alloy nanoparticles in N-doped CNT represents an effective way to fine tuning of the electron interactions between encapsulated nanoparticles and CNTs, and hence generate rich active sites for electrocatalysis [30].

Prior researches reveal that N,S-codoped carbon materials generally showed better catalytic activity than the N-doped only carbons due to the synergistic effects of nitrogen and sulfur dopants [31,32]. Therefore, one straight question arises. How is the electrocatalytic performance of metal or metal-alloy nanoparticles encapsulated by N,S-codoped CNTs? This is the primary motivation of present work.

Herein, a series of noble metal-free electrocatalysts, that is iron-cobalt alloy nanoparticles encapsulated in nitrogen and sulfur co-doped carbon nanotubes (FeCo@N,S-CNTs), are synthesized by pyrolysis of Fe,Co-containing Prussian blue analogues supported on trithiocyanuric acid (TCA) aggregates in an argon atmosphere. Electrochemical studies reveal that the as-synthesized nanocomposites display a superior catalytic activity towards ORR, along with higher operation stability and stronger immunity to the crossover of methanol fuel, as compared with commercial Pt/C catalysts in alkaline electrolyte solution.

2. Experimental section

2.1. Synthesis of $Fe_3[Co(CN)_6]_2$/TCA precursor

$Fe_3[Co(CN)_6]_2$/TCA was typically synthesized as follows: 0.40 mmol $K_3[Co(CN)_6]$ was dissolved in 40.00 mL of distilled water under mechanical stirring to form a homogeneous solution. Then 20.00 mL of distilled water containing 0.60 mmol $FeCl_2$ and 0.500 g surfactant polyvinyl pyrrolidone (PVP) was mixed with the above $K_3[Co(CN)_6]$ aqueous solution slowly with a syringe to form a faint yellow colloid solution. The reaction was allowed to proceed at room temperature with magnetic stirring for about 1 h. Subsequently, 60.00 mL of DMF solution containing 2.000 g TCA was added dropwise into the above reaction solution and further stirred for about 5.0 h. Finally, the resulting yellow precipitates denoted as $Fe_3[Co(CN)_6]_2$/TCA were filtered and washed several times with distilled water and then dried under a vacuum oven at 60.0 °C for overnight. $Fe_3[Fe(CN)_6]_2$/TCA and $Co_3[Co(CN)_6]_2$/TCA were prepared in a similar procedure by replacing $K_3[Co(CN)_6]$ and $FeCl_2$ with $K_3[Fe(CN)_6]$ and $CoCl_2$, respectively. To synthesize Fe,Co-containing melamine composites, 0.500 g $Fe_3[Co(CN)_6]$ and 2.000 g melamine were mixed in 50.00 mL of ethanol at room temperature under magnetic stirring, and then methanol was evaporated by heating up the solution to 60.0 °C.

2.2. Synthesis of FeCo@N,S-CNT

FeCo@N,S-CNTs were synthesized by one-step heat treatment with $Fe_3[Co(CN)_6]_2$/TCA precursor according to the methods reported elsewhere [21,33,34], where TCA was used as carbonaceous source, sulfur source and also nitrogen source, while $Fe_3[Co(CN)_6]_2$ was used as a catalyst for the growth of CNTs. 0.500 g $Fe_3[Co(CN)_6]_2$/TCA was placed in a porcelain boat, then heated up to 800.0 °C at a ramping rate of 5.0 °C/min, and then maintained at 800.0 °C for 120.0 min under N_2 protection. The resulting black product was repeatedly washed with 0.1 M HCl solution for 5.0 h and dried under vacuum at 70.0 °C for overnight, affording the FeCo@N,S-CNT-800 sample. Similarly, control samples were also prepared at 700.0 °C and 900.0 °C in the same fashion, leading to FeCo@N,S-CNT-700 and FeCo@N,S-CNT-900, respectively. The whole synthesis process is schematically illustrated in Scheme 1. Fe@N,S-CNTs, Co@N,S-CNTs and FeCo@N-CNTs were prepared in a similar fashion by using $Fe_3[Fe(CN)_6]_2$/TCA, $Co_3[Co(CN)_6]_2$/TCA and $Fe_3[Co(CN)_6]_2$/melamine as precursors for direct pyrolysis, respectively.

2.3. Characterization

Transmission electron microscopy (TEM) measurements were carried out on a Tecnai G2-F20 integrated with an EDS analyzer, and the acceleration voltage was 100 kV. Scanning electron microscopy (SEM) measurements were conducted with a field-emission scanning electron microscope (S-4800, Hitachi). The chemical states and component contents of samples were analyzed by X-ray photoelectron spectroscopy (XPS) measurement with a Phi X-tool instrument. During measurements, C1s at 284.5 eV was used as an internal reference to calibrate all the XPS curves. Before conducting quantitative analysis, a stable chemical compound with a definite stoichiometric ratio, for example anhydrous Na_2SO_4 (99.999% metals basis, Aladdin Regent, China), was used as a reference to calibrate the XPS instrument by determining the atomic ratio of Na:S:O. The corresponding XPS spectra were analyzed using XPSPeak41 software with a Gaussian (Y%)–Lorentzian parameter of 80%. Wide-angle X-ray diffraction (XRD) patterns were acquired on a Bruker D8-Advance diffractometer with Cu Kα as radiation beam. Thermogravimetric analysis (TGA) was implemented with a METTLER equipment in air at a heating rate of 5.0 °C/min. Brunauer–Emmet–Teller (BET) surface area was evaluated by measuring the nitrogen adsorption/desorption isotherm at 77.0 K with a Micromeritics ASAP 2010 instrument according to the Barrett–Joyner–Halenda (BJH) method.

2.4. Electrochemical measurements

The three-electrode half-cell measurements were performed on a CHI 750E electrochemical workstation (Chenhua Co., China), with a platinum wire serving as the counter electrode, an Ag/AgCl electrode in saturated KCl aqueous solution as the reference electrode, and a glassy carbon electrode (GCE) (diameter: 5.0 mm) loaded with catalysts as the working electrode. Before deposition, the catalysts were dispersed into a homogeneous solution containing deionized water, isopropanol and commercial nafion (5.0 wt %) at a volume ration of 4:1:0.025 to form a homogeneous suspension with a catalyst concentration of 2.0 mg/mL. To prepare a catalyst-modified electrode, 20.0 μL of the catalyst suspension was evenly casted on the surface of pre-cleaned GCE with a micropipet and then dried in air at room temperature, affording a catalyst loading of 200 μg/cm^2. The commercial Pt/C-modified electrode was also prepared in the same fashion with a catalyst loading of 100 μg/cm^2. Linear sweep voltammograms (LSV) at various rotating speeds (400–2025 rpm) were acquired in 0.1 M KOH aqueous

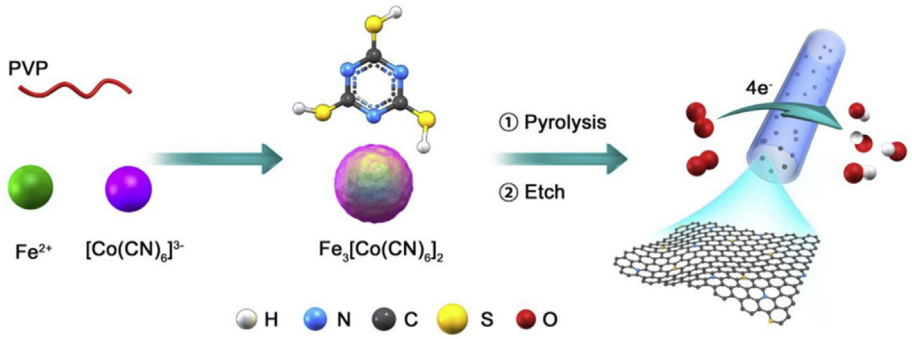

Scheme 1. A schematic introduction to the synthesis of FeCo@N,S-CNT samples.

solution saturated with O_2.

The Koutecky–Levich (K-L) plots were drawn and analyzed with the following equations:

$$j^{-1} = j_L^{-1} + j_k^{-1} = (Bw^{1/2})^{-1} + j_k^{-1} \quad (1)$$

$$B = 0.62nFC_0(D_0)^{2/3}v^{-1/6}$$

$$j_k^{-1} = nFkC_0$$

where j is the apparent current density, j_k corresponds to the kinetic current density; j_L is the diffusion current density; w is the rotation rate of electrode; F is the Faraday constant (96485 C mol^{-1}); C_0 of 1.2×10^{-6} mol cm^{-3} and D_0 of 1.9×10^{-5} cm^2 s^{-1} is the solubility and diffusion coefficient of O_2 in water at room temperature, respectively; k is the rate constant of electron transfer, and v is the kinematic viscosity of electrolyte (ca. 0.01 cm^2 s^{-1}).

3. Results and discussion

Fig. 1a shows the representative SEM image of FeCo@N,S-CNT-800 that was prepared by direct pyrolysis of $Fe_3[Co(CN)_6]_2$/TCA (Fig. S1) at 800.0 °C, where a large number of randomly distributed tubular nanostructures with open ends are observed. Interestingly, tubular nanostructures were also observed for the series control samples denoted as Fe@N,S-CNT-800, Co@N,S-CNT-800 and FeCo@N-CNT-800 in Fig. S2. These tubular structures are attributed to CNTs, and the diameters for FeCo@N,S-CNT-800 are mostly within the range of ca. 15.00 nm to 100.00 nm while the amount of CNTs and their lengths are dependent on annealing temperature. As shown in Fig. S3, only a small number of CNTs were observed for FeCo@N,S-CNT-700 as compared with FeCo@N,S-CNT-800. However, no apparent increment of CNT content but slight aggregation/entanglement was observed when the pyrolysis temperature was further increased to 900.0 °C. As for the length of CNTs, it steadily increased from submicron scale for FeCo@N,S-CNT-700 to several microns for FeCo@N,S-CNT-800, and then showed a plateau for FeCo@N,S-CNT-900. Careful observations reveal that most of these CNTs show a peapod-like morphology. Indeed, from the corresponding TEM image of FeCo@N,S-CNT-800 (Fig. 1b), peapod-like CNTs are clearly identified with a predominant diameter of ca. 50.00 nm. Additionally, in the low-contrast CNTs are distributed a number of dark-contrast nanoparticles. Statistic analysis based on more than one hundred such dark-contrast nanoparticles showed that the nanoparticles were mostly 9.00 ± 0.21 nm in diameter, as manifested in the core-size histogram in Fig. S4. From the higher-magnification TEM image, one can find that such nanoparticles were actually encapsulated by several thin carbon layers (Fig. 1c). Furthermore, the corresponding high-resolution TEM image (Fig. 1d) showed that the thickness of such a thin carbon layer was about 2.60 nm, and the thin carbon layer was virtually comprised with a few wavy sub-layers with a spacing of 4.00 Å, suggesting the formation of graphitic interlayers. In addition, well-defined lattice fringes with a d-spacing of 2.02 Å are observed on the dark-contrast nanoparticles (Fig. 1d), corresponding to the (110) plane of FeCo alloy [35]. These observations signify the formation of crystalline FeCo alloy nanoparticles encapsulated in thin CNTs. Note that no crystalline metal sulfide was observed though the precursor had a high content of sulfur element. The presence of thin carbon encapsulating layer on FeCo may not only prevent the alloy nanoparticles from corrosion and oxidation but also remarkably improve the stability of catalysts and avoid particle aggregation issues in operation.

Raman spectra of FeCo@N-CNT-800 and FeCo@N,S-CNT-800 were showed in Fig. S5 where two well-resolved peaks at around 1350.0 and 1580.0 cm^{-1} were observed, ascribing to the D and G band, respectively. Generally, the D band is derived from the defects in graphitic skeletons, while the G band is resulting from the highly ordered graphitization structure [36]. Interestingly, the intensity ratio of D and G bands (I_D/I_G) is increased from 1.11 for FeCo@N-CNT-800 to 1.14 for FeCo@N,S-CNT-800, and the full width at half maximum (FWHM) of G band, another important parameter for evaluating the degree of defects for graphene, of FeCo@N-CNT-800 is less than that of FeCo@N,S-CNT-800. These observations indicate that further doping of N-CNTs with S element leads to more defects on carbon skeletons. Consequently, the crystallinity of N-CNTs is decreased after further incorporation of S dopant onto the honeycomb-like carbon skeletons. Additionally, no peak can be observed in the Raman spectra from 300 to 600 cm^{-1}, indicative of only trace amount of FeOx (if any) in both FeCo@N-CNT-800 and FeCo@N,S-CNT-800 samples.

To track the distribution of different elements in FeCo@N,S-CNT-800, high-angle annular dark-field scanning transmission electron microscopy (HAADF-STEM) measurements were conducted, where N, S, Fe and Co elements were found to uniformly distribute on the entire sample (panels 3–6 in Fig. 1e). Interestingly, marked resemblance was observed between the distributions of Fe and Co, indicating that Fe and Co present in the same compound. On basis of the elemental mapping results, it is found that the content of Fe is apparently higher than that of Co. This conclusion is further supported by the EDS measurements (Fig. S6), where the average element content is determined to be 66.15 at.% for C, 17.62 at.% for N, 1.31 at.% for S, 5.60 at.% for Fe, 4.39 at.% for Co and 4.91 at. % for O. Note that such a high content of nitrogen dopants in FeCo@N,S-CNT-800 may increase the conductivity of CNTs and concurrently form large amounts of active sites to drastically improve the ORR catalytic performance [37].

XRD measurements were then conducted to study the

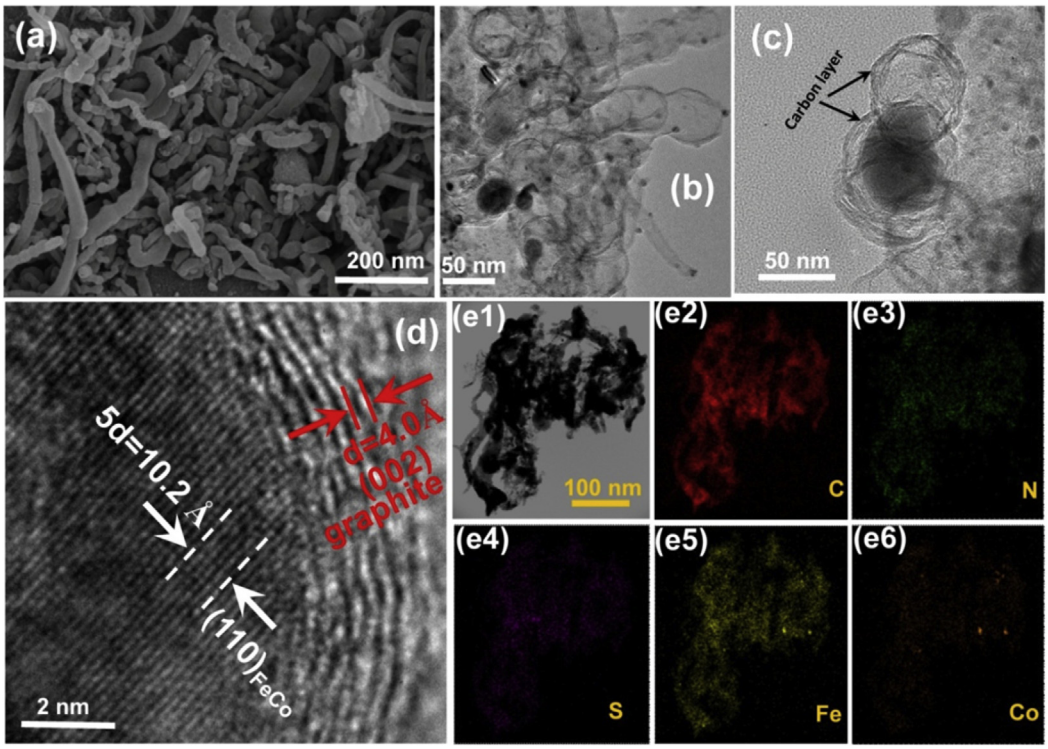

Fig. 1. (a) SEM image, (b, c) TEM images and (d) high-resolution TEM image of FeCo@N,S-CNT-800. (e1) High-angle annular dark field (HAADF)-STEM image of FeCo@N,S-CNT-800 and the corresponding elemental mapping images for (e2) C, (e3) N, (e4) S, (e5) Fe, and (e6) Co, respectively.

crystalline structures of FeCo@N,S-CNT-T (T = 700, 800, 900) composites. As depicted in Fig. 2a, a broad diffraction peak centered at 2θ = 26.1° is observed for all the three FeCo@N,S-CNT composites, which is ascribed to the (002) plane of graphite. In addition, three pronounced diffraction peaks are identified at 2θ of 44.8°, 65.3° and 82.6°, corresponding to the (110), (200) and (211) planes of body centered cubic (bcc) phase of FeCo alloy (JCPDS#49-1567) [35,38,39], respectively. Based on the calculation according to

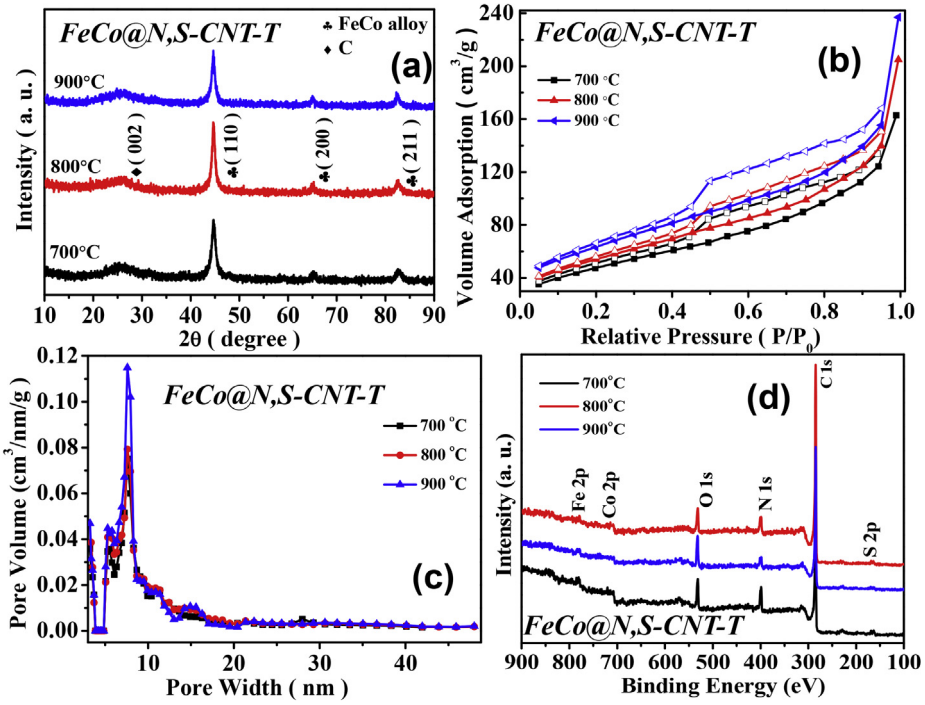

Fig. 2. (a) XRD patterns, (b) Nitrogen adsorption–desorption isotherms, (c) the corresponding pore-size distribution and (d) XPS spectra for FeCo@N,S-CNT-T (T = 700.0, 800.0, 900.0 °C).

Scherrer equation, the lateral size of FeCo crystallites along the crystallographic [110] direction is about 8.50 ± 0.35 nm for FeCo@N,S-CNT-800 sample, which is very close to the statistic value (9.00 ± 0.21 nm) of TEM measurements in Fig. S4b. These observations further confirm the formation of crystalline FeCo alloy nanoparticles in FeCo@N,S-CNT composites by facile pyrolysis of the $Fe_3[Co(CN)_6]_2$/TCA precursor. Again, no crystalline metal sulfide was found. TGA conducted in oxygen revealed two apparent weight-loss regions for FeCo@N,S-CNT-800 sample (Fig. S4a). The first weight loss of ca. 7.5% appeared below 100 °C was ascribed to the evaporation of adsorbed water. The sudden weight loss of about 44.5% emerged at around 390 °C, which is due to the oxidation removal of CNTs. Calculations suggest that the loading of FeCo nanoparticle alloy in CNTs is about 34.0 wt%. Note that the contents of metals or metal alloys for all the investigated samples are about 30 wt% (Fig. S4a), except for commercial Pt/C (20 wt%) catalyst.

The specific surface area and correlated pore structure of FeCo@N,S-CNT composites were studied by BET measurements. As depicted in Fig. 2b, all the N_2 adsorption/desorption isotherms depict a hysteresis loop between the relative pressure P/P_0 of 0.40−0.95, coinciding with the type-IV isotherms. One can find that the adsorption volume of FeCo@N,S-CNT composites increases with increasing the pyrolysis temperature, with a calculated specific surface area of 171.46 m^2/g for FeCo@N,S-CNT-700, 195.16 m^2/g for FeCo@N,S-CNT-800 and 228.58 m^2/g for FeCo@N,S-CNT-900. For the three corresponding pore size distribution plots in Fig. 2c, they show high resemblance to each other, with a predominant mesopore size of about 7.59 nm for all the three FeCo@N,S-CNT samples. Comparable pore sides are also observed for control samples FeCo@N-CNT, Fe@N,S-CNT and Co@N,S-CNT (Fig. S7).

The elemental valence states and surface compositions of FeCo@N,S-CNT composites were analyzed by XPS measurements. As shown in Fig. 2d, the peaks ascribed to elements C, S, N, O, Fe and Co were clearly identified in the XPS survey spectra of the three FeCo@N,S-CNT-T composites. As for FeCo@N,S-CNT-800, the content of element was evaluated by the integrated area of corresponding peaks, which is 73.64 at.% for C, 9.96 at.% for N, 13.32 at.% for O, 1.52 at.% for S, 0.84 at.% for Fe and 0.72 at.% for Co. Note that the contents of Fe and Co elements determined by XPS, a surface sensitive technique, are much lower than that evaluated by conventional EDS and TGA measurements, which indicate that the FeCo alloy is virtually encapsulated by carbon layers, coinciding with the TEM results.

For the high-resolution spectrum of N1s electron (Fig. 3a), it can be deconvoluted into three distinct peaks centered at about 398.0 eV, 400.1 eV and 401.3 eV, ascribing to pyridinic N, pyrrolic N and graphitic N, respectively [40]. Although the total nitrogen content decreases from 12.38 at% for FeCo@N,S-CNT-700 to 9.96 at% for FeCo@N,S-CNT-800 and 3.91 at% for FeCo@N,S-CNT-900, the content of both pyridinic-N and graphitic-N remains over 70% of the total nitrogen dopants for the three FeCo@N,S-CNT-T composites (Table 1 and Fig. S8). The decrease of total nitrogen content with increasing temperature is attributed to the release of nitrogen dopants due to graphitization of carbonaceous precursors during pyrolysis. Because graphitic N and pyridinic N are generally considered as the potential ORR active sites for N-doped carbons [9,41,42], the retention of a high content of both graphitic N and pyridinic N may lead to high ORR activity for FeCo@N,S-CNT-T composites.

In addition, deconvolution of the high-resolution S2p XPS spectrum yields two apparent peaks at about 163.7 eV and 168.7 eV (Fig. 3b), corresponding to S in -C-S-C- and $-SO_n-$, respectively [43]. The presence of -C-S-C- bonding configuration confirms the successful doping of sulfur into carbon nanotubes [44,45]. For the high-resolution XPS spectrum of Co2p electrons (Fig. 3c), it can be deconvoluted into seven peaks, where the three peaks at 778.1, 781.1 and 783.1 eV are corresponding to Co^0 [46,47] while the other four peaks at about 780, 782.1, 785.5, and 786.5 eV, are ascribed to the peaks of CoO. As for the high-resolution Fe2p spectrum (Fig. 3d), it can be deconvoluted into eight peaks, where the peaks at about 708.4 and 709.2eV are attributed to Fe^{2+} in Fe_3O_4, the peaks at about 710.2, 711.2, 712.3, 713.4 and 714.5 eV are corresponding to Fe^{3+} in Fe3O4, while the peak at 706.7 eV is ascribed to Fe^0 [47–49]. Taken together, the XPS results signify the successful preparation of N, S-codoped CNT composites with FeCo alloy.

The ORR activity of composite catalysts was studied by rotating ring-disk electrode (RRDE) technique in O_2-saturated electrolyte solution (0.1 M KOH) at room temperature. As shown in Fig. 4a, the cathodic current for all three FeCo@N,S-CNT-T samples started to increase abruptly when the electrochemical potential was negatively scanned across +0.980V (vs. RHE) for FeCo@N,S-CNT-800 and + 0.960 V for both FeCo@N,S-CNT-700 and FeCo@N,S-CNT-900, suggesting that lower overpotential is required for FeCo@N,S-CNT-800 to catalyze ORR among the series. Accordingly, the half-wave potential was determined to be +0.816 V (vs. RHE) for FeCo@N,S-CNT-700, +0.838 V for FeCo@N,S-CNT-800 and + 0.814 V for FeCo@N,S-CNT-900, again indicative of a highest ORR activity for FeCo@N,S-CNT-800 among the series of samples prepared at varied thermal annealing temperature. The diffusion-limiting current was found to steadily decrease with increasing the pyrolysis temperature, with 5.331 mA/cm^2 for FeCo@N,S-CNT-700, 5.163 mA/cm^2 for FeCo@N,S-CNT-800 and 4.471 mA/cm^2 for FeCo@N,S-CNT-900 at +0.500 V (vs. RHE). This coincides with the evolution of total nitrogen content for CNTs in Table 1, where increase of the pyrolysis temperature causes continuous decrease in the content of overall nitrogen dopants. These results suggest that the optimized temperature for preparing FeCo@N,S-CNT based ORR electrocatalysts is approximately 800 °C.

A series of control experiments were also conducted to study the synergetic effects of multiple dopants on ORR activity. As shown in Fig. 4b, the introduction of Fe-containing salts into the precursors substantially enhanced the ORR activity of N,S-codoped carbon catalysts. Specifically, the onset potential was found to increase from +0.914 V (vs. RHE) for N,S-C to +0.954 V for Fe@N,S-CNT-800. Similarly, introduction of Co element in precursors also substantially enhanced the ORR activity. For example, besides the highly comparable onset potential and diffusion-limiting current density, a higher half-wave potential of +0.807 V (vs. RHE) was observed for Co@N,S-CNT-800, as compared to the +0.787 V for Fe@N,S-CNT-800. Interestingly, although the total weight content of metal elements were remained virtually unchanged, concurrent introduction of both Fe and Co elements remarkably improved the ORR activity compared to that prepared with single transition metal element (Fe or Co) in the precursor, in terms of onset potential, half-wave potential and diffusion-limiting current density. These results manifest the positively synergetic effect of Fe and Co elements on the ORR activity metal nanocrystals encapsulated in N,S-CNTs. However, compared to metal doping, more significant impacts on the ORR activity of FeCo@CNT catalysts were observed in sulfur doping. From Fig. 4b, the onset potential, half-wave potential and limiting-current density at +0.500 V were determined to be +0.954 V, +0.738 V and 3.764 mA/cm^2, respectively, for the N-doped only sample FeCo@N-CNT-800. Whereas, further introducing sulfur element into the precursor led to sulfur and nitrogen codoped sample FeCo@N,S-CNT-800 with a drastically enhanced onset potential of +0.980 V, a half-wave potential of +0.838 V and a limiting-current density of 5.500 mA/cm^2 at +0.500 V. Normally, high conductivity is beneficial to oxygen reduction reaction because it can accelerate the electron transfer process. As for the electrochemical impedance spectroscopy (EIS) measurements,

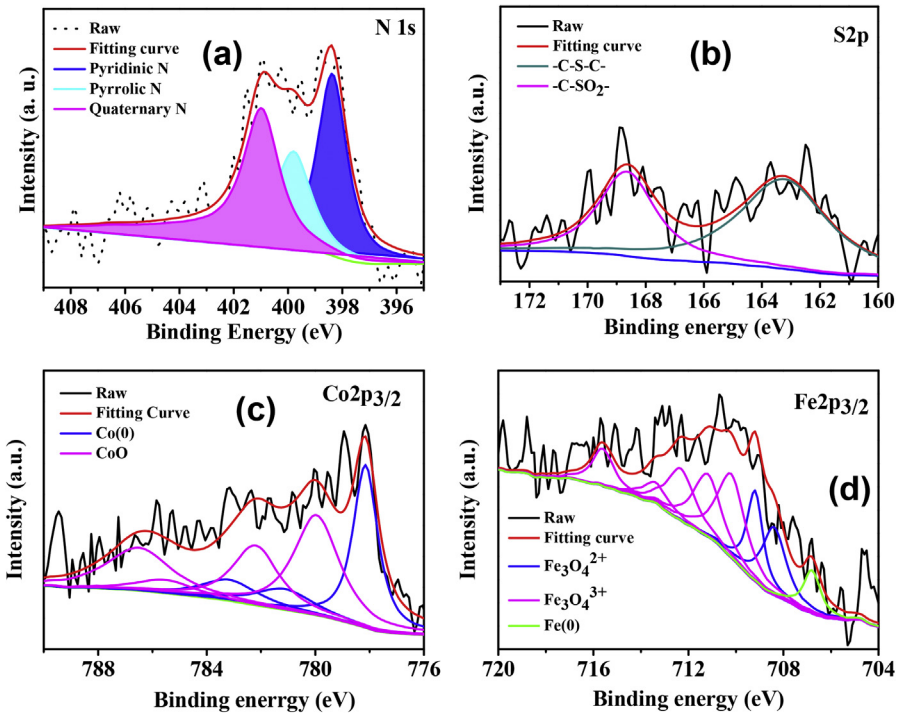

Fig. 3. High-resolution XPS spectrum of (a) N1s, (b) S2p, (c) Co2p3/2 and (d) Fe2p3/2 electrons for FeCo@N,S-CNT-800 sample.

Table 1
Summary of the details of pore structure determined by BET measurments and surface composition content of catalysts determined by XPS.

Sample Name	BET Surface Area (m^2/g)	Dominant Pore Size (nm)	C at.%	O at.%	S at.%	N at.%			Fe at.%	Co at.%
						Pyridinic N	Pyrrolic N	Graphitic N		
FeCo@N,S-CNT-700	171.46	7.59	72.07	11.91	1.82	5.76	6.00	0.62	0.52	1.30
FeCo@N,S-CNT-800	195.16	7.59	73.64	13.32	1.52	3.83	2.36	3.77	0.84	0.72
FeCo@N,S-CNT-900	228.58	7.59	68.54	25.03	0.26	0.87	1.03	2.01	1.52	0.74

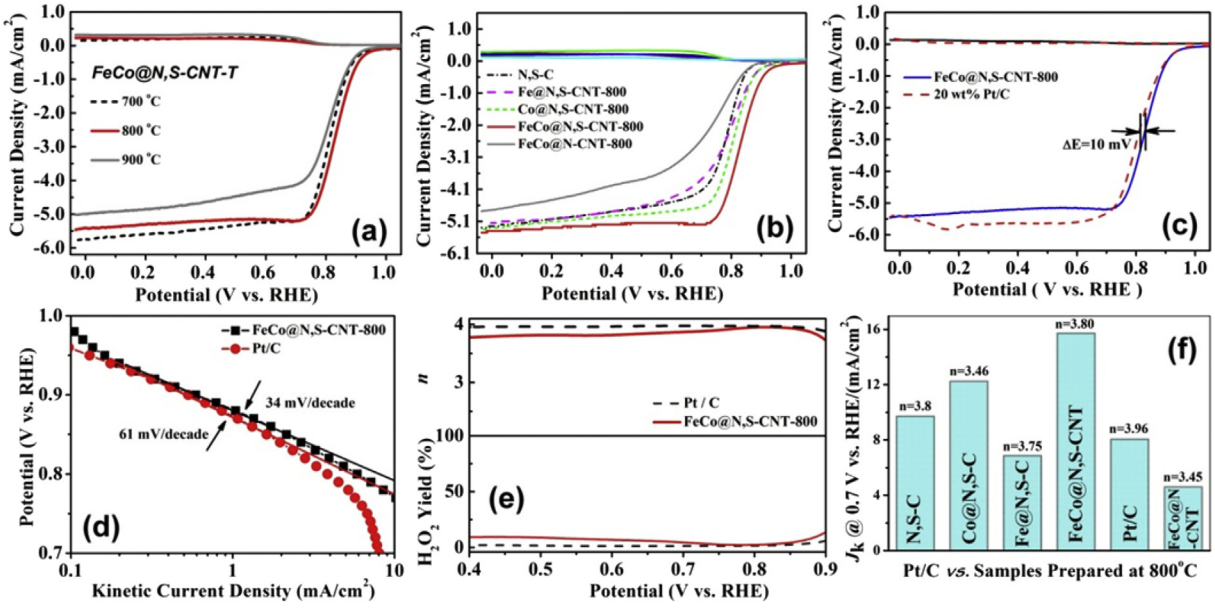

Fig. 4. LSV for (a) FeCo@N,S-CNT-T (T = 700, 800, 900), (b) N,S-C-800, Fe@N,S-C-800, Co@N,S-C-800,FeCo@N,S-CNT-800 and FeCo@N-CNT-800 at a rotation rate of 1600 rpm in O_2-saturated 0.1 M KOH solution. (c) Comparison of LSV for Pt/C and FeCo@N,S-CNT-800. (d) Corresponding Tafel plot of Pt/C and FeCo@N,S-CNT-800. (e) The plots of electron-transfer number *n* and H_2O_2 yield of Pt/C and FeCo@N,S-CNT-800 as a function of electrode potential. (f) The histograms of kinetic current density J_k at +0.700 V for different samples.

analysis of EIS at high-frequency region (inset to Fig. S9) suggests that the intrinsic resistance in FeCo@N,S-CNT-800 is comparable to that of Co@N,S-CNT-800 and FeCo@N-CNT-800 but slightly lower than that of Fe@N,S-CNT-800, as signified by the nearly comparable slopes for FeCo@N,S-CNT-800, Co@N,S-CNT-800 and FeCo@N-CNT-800 while a somewhat lower slope is observed for Fe@N,S-CNT-800. In low-frequency region, the diameter of semicircle for FeCo@N,S-CNT-800 is observed to be much smaller than that for Fe@N,S-CNT-800 and Co@N,S-CNT-800, which reveals that the charge transfer resistance in FeCo@N,S-CNT-800 is remarkably reduced as compared with that of Fe@N,S-CNT-800 and Co@N,S-CNT-800, coinciding with a higher ORR activity for FeCo@N,S-CNT-800 than that observed for Fe@N,S-CNT-800 and Co@N,S-CNT-800. However, the charge transfer resistance of FeCo@N,S-CNT-800 is found to be higher than that of FeCo@N-CNT-800 while the ORR activity for these two samples is in a converse order, which indicates that, compared with defects/dopants, the influence of interfacial conductivity on the ORR catalytic activity is not so significant. Therefore, FeCo@N-CNT-800 showed the lowest ORR activity among all the investigated samples.

Actually, the activity of FeCo@N,S-CNT-800 composite is highly comparable to that of commercial Pt/C catalyst in ORR catalysis. As depicted in Fig. 4c, although FeCo@N,S-CNT-800 showed a slightly lower limiting current and the same onset potential value as compared with commercial Pt/C catalysts, FeCo@N,S-CNT-800 catalyst displayed a more positive half-wave potential of +0.838 V than the +0.828 V of commercial Pt/C catalyst. For the correlated Koutecky–Levich (K–L) plots for FeCo@N,S-CNT-800 shown in Fig. S10, linear fittings with highly comparable slopes were observed between +0.400 V and +0.700 V, which indicates that ORR on FeCo@N,S-CNT-800 follows a first-order kinetics with respect to the concentration of oxygen in electrolyte solution. In the corresponding Tafel plots (Fig. 4d), a slope of ca. 61 mV/decade was determined for Pt/C, while only 30 mV/decade was identified for FeCo@N,S-CNT-800, indicating the first-electron reduction of oxygen dominates the ORR process. Importantly, the specific catalytic activity of FeCo@N,S-CNT-800 was clearly superior to that of Pt/C within the potential range from +0.700 to +0.980 V.

The number of electron transfer (n) and H_2O_2 yield were calculated with the disk and ring currents according to the following eq. (2) and eq. (3), respectively.

$$n = \frac{4\boldsymbol{I_d}}{\boldsymbol{I_d} + \boldsymbol{I_r}/\boldsymbol{N}} \tag{2}$$

$$H_2O_2\% = \frac{200\boldsymbol{I_r}/\boldsymbol{N}}{\boldsymbol{I_r}/\boldsymbol{N} + \boldsymbol{I_d}} \tag{3}$$

where I_d is the disk current density, I_r is the corresponding ring current density and N is the current collection efficiency (0.37) of Pt ring.

From Fig. 4e, one can find that although n of the FeCo@N,S-CNT-800 catalyst is slightly lower than that of Pt/C, it is close to 4 within the potential range from +0.400 V to +0.900 V (vs. RHE), indicating that FeCo@N,S-CNT-800 has a high selectivity towards $4e^-$ reduction of oxygen. The corresponding H_2O_2 yield for FeCo@N,S-CNT-800 is determined to vary between 6.88% and 1.50% in the low overpotential range from +0.600 V to +0.850 V, which is highly comparable to that of commercial Pt/C catalyst. Note that in this low overpotential region the kinetic current and n number of FeCo@N,S-CNT-800 are much higher than those of the control samples (Fig. 4f). Furthermore, although the n number of FeCo@N,S-CNT-800 catalyst (3.80) is lower than that of Pt/C (3.96) at +0.700 V, a remarkably higher kinetic current density of 15.72 mA/cm^2 is observed for the FeCo@N,S-CNT-800 catalyst at the same potential compared to the 8.050 mA/cm^2 for Pt/C catalyst, again indicative of an efficient ORR activity for FeCo@N,S-CNT-800 catalyst.

Since Fe and Co elements usually form M-N_x-C (M = Fe and Co) species which are reported to constitute partial ORR active sites in the extensively investigated M-N/C catalysts [49–51], therefore one may ask what roles FeCo alloy play in catalyzing ORR. To shed light on this question, control experiments were conducted. It is well documented that nitrite (NO_2^-), cyanide (CN^-) or sulfur cyanide (SCN^-) ions can strongly coordinate with Fe- or Co-containing compounds and hence cause drastic decrease in catalytic activity [52]. As shown in Fig. 5a, the presence of 10 mM KSCN (red curve) only caused ca. 10 mV negative shift in the half-wave potential while the limiting current was nearly unchanged, as compared with that without the addition of KSCN. These observations unravel two important results. One is that the content of M-N_x-C (M = Fe and Co) moieties on the surface of CNTs, if any, is negligible and their contributions to ORR are trivial. Another is that the FeCo-alloy nanocrystals are nearly completely encapsulated in N,S-CNTs that not only help prevent the FeCo-alloy nanocrystals from poisoning and corroding but also impede their aggregation during operation. Moreover, electron transfer from the encapsulated FeCo alloy nanoparticles to thin walls of CNTs may occur, which lowers the local work function of CNTs and notably facilitates the adsorption of O_2 as well as its breaking to from -OH [28,53]. This charge transfer state is reported to intensify upon doping exterior carbon walls with nitrogen [28]. Because sulfur has a comparable electron affinity to that of carbon, sulfur dopant on carbon skeleton might donate its lone pair electrons to the p_z of adjacent carbon atoms, which is favorable to both the electrostatic and covalent bonding of O_2 onto the carbon layer encapsulating metallic FeCo alloy, and hence it is expected to remarkably enhance the ORR activity by further introduction of sulfur dopants besides nitrogen, as corroborated by the electrochemical results in Fig. 4b. Taken together, it can be concluded that sulfur doping substantially enhances the ORR catalytic activity of FeCo-alloy nanocrystals encapsulated in CNTs, where the ORR activity is mainly derived from the electronic interactions between encapsulated FeCo-alloy nanocrystals and thin walls of N,S-CNTs.

In addition, the encapsulation of FeCo nanocrystals with thin CNTs greatly enhanced the tolerance to fuel crossover effect. As shown in Fig. 5b, for the commercial Pt/C (20 wt%) catalyst, the addition of methanol caused a sudden complete loss of cathodic current due to the formation of mixed potentials deriving from the emergence of methanol oxidation on cathode. After continuous operation for about 2000s, the cathodic current recovered to ca. 80% of its initial value. Whereas, a slight increase of the cathodic current for FeCo@N,S-CNT-800 modified electrode was observed after the addition of methanol to electrolyte likely due to agitation during methanol addition. The completely different response of cathodic current to methanol for FeCo@N,S-CNT-800 modified electrode indicates that FeCo@N,S-CNT-800 is virtually immune to fuel crossover effect, a highly preferred capability for catalysts in practical electrochemical energy conversion/storage devices.

The operation stability of catalysts was evaluated by the decay of cathodic current as a function of time in chronoamperometric measurements. As displayed in Fig. 5c, after continuously working in the 0.1 M KOH aqueous solution for 30000s the cathodic current of commercial Pt/C (20 wt%) catalyst gradually declined to ca. 85% of its initial value, which is much lower than the 97% observed for FeCo@N,S-CNT-800 in the same measurement conditions. This observation highlights the superior operation stability of FeCo@N,S-CNT-800, as compared to that of commercial Pt/C catalyst.

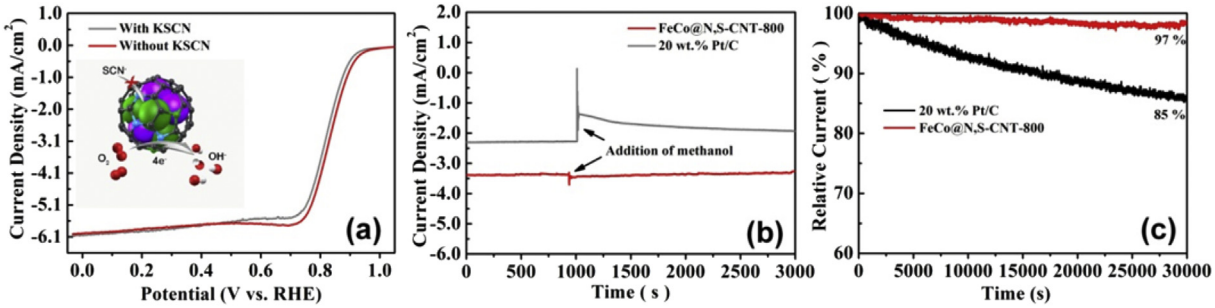

Fig. 5. (a) LSV curves of FeCo@N,S-CNT-800 and in 0.1 M KOH aqueous solution with the addition of 10 mM KSCN. (b) Chronoamperometric curves of a glassy-carbon electrode modified with catalysts at +0.700 V vs RHE in an O_2-saturated 0.1 M KOH solution with 3 M methanol addition at 1000s. Electrode rotation rate was 900 rpm. (c) Current–time chronoamperometric responses of Pt/C and FeCo@N,S-CNT-800 at +0.700 V vs RHE in an O_2-saturated 0.1 M KOH solution. Electrode rotation rate was 900 rpm.

4. Conclusions

In summary, metal alloy nanoparticles encapsulated in nitrogen and sulfur-codoped peapod-like carbon nanotubes with a diameter within the range of ca. 15 nm to 100 nm were prepared by direct pyrolysis of the $Fe_3[Co(CN)_6]_2$/TCA precursor. Electrochemical measurements revealed that further introduction of sulfur dopant onto the surface of N-CNTs significantly enhanced the ORR activity of FeCo@N-CNT in alkaline electrolyte most likely due to the intensified charge transfer from encapsulated FeCo alloy nanoparticles to thin walls of CNTs. The best sample FeCo@N,S-CNT-800 exhibited a more positive half-wave potential of +0.838 V, nearly double kinetic current, as compared with the corresponding key parameters of commercial Pt/C catalysts. The encapsulation of FeCo alloy nanoparticles with thin carbon layers imparts FeCo alloy a strong immunity to fuel crossover effect and also significantly enhances the operation stability. The excellent catalytic performance observed in nitrogen- and sulfur-codoped carbon nanotubes encapsulating FeCo alloy suggest the high potential of present strategy in optimizing the catalytic performance of metal nanoparticles encapsulated in CNTs for related electrochemical energy devices.

Acknowledgements

This work was supported by the National Natural Science Foundation of China (NSFC 51402111 and 21528301), Guangdong Innovative and Entrepreneurial Research Team Program (2014ZT05N200) and the Fundamental Research Funds for the Central Universities (SCUT Grant No. 2153860).

Appendix A. Supplementary data

Supplementary data related to this article can be found at https://doi.org/10.1016/j.jallcom.2018.01.144.

References

[1] F. Cheng, J. Chen, Metal–air batteries: from oxygen reduction electrochemistry to cathode catalysts, Chem. Soc. Rev. 41 (2012) 2172–2192.
[2] H. Yu, L. Shang, T. Bian, R. Shi, G.I.N. Waterhouse, Y. Zhao, C. Zhou, L.-Z. Wu, C.-H. Tung, T. Zhang, Nitrogen-doped porous carbon nanosheets templated from g-C3N4 as metal-free electrocatalysts for efficient oxygen reduction reaction, Adv. Mater. 28 (2016) 5080–5086.
[3] W. Wang, J. Luo, W. Chen, J. Li, W. Xing, S. Chen, Synthesis of mesoporous Fe/N/C oxygen reduction catalysts through NaCl crystallite-confined pyrolysis of polyvinylpyrrolidone, J. Mater. Chem. A 4 (2016) 12768–12773.
[4] B. Men, Y. Sun, J. Liu, Y. Tang, Y. Chen, P. Wan, J. Pan, Synergistically enhanced electrocatalytic activity of sandwich-like N-Doped graphene/carbon nanosheets decorated by Fe and S for oxygen reduction reaction, ACS Appl. Mater. Interfaces 8 (2016) 19533–19541.
[5] W. Xia, A. Mahmood, Z. Liang, R. Zou, S. Guo, Earth-abundant nanomaterials for oxygen reduction, Angew. Chem. Int. Ed. 55 (2016) 2650–2676.
[6] L. Zhang, Q. Chang, H. Chen, M. Shao, Recent advances in palladium-based electrocatalysts for fuel cell reactions and hydrogen evolution reaction, Nano Energy 29 (2016) 198–219.
[7] Y. Hou, T. Huang, Z. Wen, S. Mao, S. Cui, J. Chen, Metal–Organic framework-derived nitrogen-doped core-shell-structured porous Fe/Fe 3 C@C nanoboxes supported on graphene sheets for efficient oxygen reduction reactions, Adv. Eng. Mater. 4 (2014) 1220–1225.
[8] X. Fu, J.-Y. Choi, P. Zamani, G. Jiang, M.A. Hoque, F.M. Hassan, Z. Chen, Co–N decorated hierarchically porous graphene aerogel for efficient oxygen reduction reaction in acid, ACS Appl. Mater. Interfaces 8 (2016) 6488–6495.
[9] H.B. Yang, J. Miao, S.F. Hung, J. Chen, H.B. Tao, X. Wang, L. Zhang, R. Chen, J. Gao, H.M. Chen, Identification of catalytic sites for oxygen reduction and oxygen evolution in N-doped graphene materials: development of highly efficient metal-free bifunctional electrocatalyst, Sci. Adv. 2 (2016) e1501122–e1501122.
[10] C.H. Choi, S.H. Park, S.I. Woo, Binary and ternary doping of nitrogen, boron, and phosphorus into carbon for enhancing electrochemical oxygen reduction activity, ACS Nano 6 (2012) 7084–7091.
[11] A.M. El-Sawy, I.M. Mosa, D. Su, C.J. Guild, S. Khalid, R. Joesten, J.F. Rusling, S.L. Suib, Controlling the active sites of sulfur-doped carbon nanotube–graphene nanolobes for highly efficient oxygen evolution and reduction catalysis, Adv. Eng. Mater. 6 (2016), 1501966.
[12] Z.Q. Liu, H. Cheng, N. Li, T.Y. Ma, Y.Z. Su, ZnCo2O4 quantum dots anchored on nitrogen-doped carbon nanotubes as reversible oxygen reduction/evolution electrocatalysts, Adv. Mater. 28 (2016) 3777–3784.
[13] J. Wang, Z. Wu, L. Han, R. Lin, W. Xiao, C. Xuan, H.L. Xin, D. Wang, Nitrogen and sulfur co-doping of partially exfoliated MWCNTs as 3-D structured electrocatalysts for the oxygen reduction reaction, J. Mater. Chem. A 4 (2016) 5678–5684.
[14] G. Wu, K.L. More, P. Xu, H.-L. Wang, M. Ferrandon, A.J. Kropf, D.J. Myers, S. Ma, C.M. Johnston, P. Zelenay, A carbon-nanotube-supported graphene-rich nonprecious metal oxygen reduction catalyst with enhanced performance durability, Chem. Commun. 49 (2013) 3291–3293.
[15] W. Ai, Z. Luo, J. Jiang, J. Zhu, Z. Du, Z. Fan, L. Xie, H. Zhang, W. Huang, T. Yu, Nitrogen and sulfur codoped graphene: multifunctional electrode materials for high-performance Li-ion batteries and oxygen reduction reaction, Adv. Mater. 26 (2014) 6186–6192.
[16] T.N. Ye, L.B. Lv, X.H. Li, M. Xu, J.S. Chen, Strongly veined carbon nanoleaves as a highly efficient metal-free electrocatalyst, Angew. Chem. Int. Ed. 53 (2014) 6905–6909.
[17] L. Wang, S. Dou, J. Xu, H.K. Liu, S. Wang, J. Ma, S.X. Dou, Highly nitrogen doped carbon nanosheets as an efficient electrocatalyst for the oxygen reduction reaction, Chem. Commun. 51 (2015) 11791–11794.
[18] J.P. Paraknowitsch, A. Thomas, Doping carbons beyond nitrogen: an overview of advanced heteroatom doped carbons with boron, sulphur and phosphorus for energy applications, Energy Environ. Sci. 6 (2013) 2839–2855.
[19] J. Zhang, H. Zhou, X. Liu, J. Zhang, T. Peng, J. Yang, Y. Huang, S. Mu, Keratin-derived S/N co-doped graphene-like nanobubble and nanosheet hybrids for highly efficient oxygen reduction, J. Mater. Chem. A 4 (2016) 15870–15879.
[20] H. Zhang, Z. Ma, J. Duan, H. Liu, G. Liu, T. Wang, K. Chang, M. Li, L. Shi, X. Meng, Active sites implanted carbon cages in core–shell architecture: highly active and durable electrocatalyst for hydrogen evolution reaction, ACS Nano 10 (2015) 684–694.
[21] X. Zou, X. Huang, A. Goswami, R. Silva, B.R. Sathe, E. Mikmeková, T. Asefa, Cobalt-embedded nitrogen-rich carbon nanotubes efficiently catalyze hydrogen evolution reaction at all pH values, Angew. Chem. 126 (2014) 4461–4465.
[22] H. Jin, J. Wang, D. Su, Z. Wei, Z. Pang, Y. Wang, In situ cobalt–cobalt oxide/N-doped carbon hybrids as superior bifunctional electrocatalysts for hydrogen and oxygen evolution, J. Am. Chem. Soc. 137 (2015) 2688–2694.
[23] Q. Liu, J. Jin, J. Zhang, NiCo2S4@ graphene as a bifunctional electrocatalyst for oxygen reduction and evolution reactions, ACS Appl. Mater. Interfaces 5 (2013) 5002–5008.

[24] Z. Wang, B. Li, X. Ge, F. Goh, X. Zhang, G. Du, D. Wuu, Z. Liu, T. Andy Hor, H. Zhang, Co@ Co3O4@ PPD core@ bishell nanoparticle-based composite as an efficient electrocatalyst for oxygen reduction reaction, Small 12 (2016) 2580–2587.
[25] C.Y. Su, H. Cheng, W. Li, Z.Q. Liu, N. Li, Z. Hou, F.Q. Bai, H.X. Zhang, T.Y. Ma, Atomic modulation of FeCo–nitrogen–carbon bifunctional oxygen electrodes for rechargeable and flexible all-solid-state zinc–air battery, Adv. Eng. Mater. 7 (2017), 1602420.
[26] P. Cai, S. Ci, E. Zhang, P. Shao, C. Cao, Z. Wen, FeCo alloy nanoparticles confined in carbon layers as high-activity and robust cathode catalyst for Zn-Air battery, Electrochim. Acta 220 (2016) 354–362.
[27] J. Deng, L. Yu, D. Deng, X. Chen, F. Yang, X. Bao, Highly active reduction of oxygen on a FeCo alloy catalyst encapsulated in pod-like carbon nanotubes with fewer walls, J. Mater. Chem. A 1 (2013) 14868–14873.
[28] D. Deng, L. Yu, X. Chen, G. Wang, L. Jin, X. Pan, J. Deng, G. Sun, X. Bao, Iron encapsulated within pod-like carbon nanotubes for oxygen reduction reaction, Angew. Chem. Int. Ed. 52 (2013) 371–375.
[29] Y. Hou, S. Cui, Z. Wen, X. Guo, X. Feng, J. Chen, Strongly coupled 3D hybrids of N-doped porous carbon nanosheet/CoNi alloy-encapsulated carbon nanotubes for enhanced electrocatalysis, Small 11 (2015) 5940–5948.
[30] Q. Li, H. Pan, D. Higgins, R. Cao, G. Zhang, H. Lv, K. Wu, J. Cho, G. Wu, Metal–organic framework-derived bamboo-like nitrogen-doped graphene tubes as an active matrix for hybrid oxygen-reduction electrocatalysts, Small 11 (2015) 1443–1452.
[31] S.N. Bhange, S.M. Unni, S. Kurungot, Nitrogen and sulphur co-doped crumbled graphene for the oxygen reduction reaction with improved activity and stability in acidic medium, J. Mater. Chem. A 4 (2016) 6014–6020.
[32] T. Sun, Q. Wu, Y. Jiang, Z. Zhang, L. Du, L. Yang, X. Wang, Z. Hu, Sulfur and nitrogen codoped carbon tubes as bifunctional metal-free electrocatalysts for oxygen reduction and hydrogen evolution in acidic media, Chem. A Eur. J. 22 (2016) 10326–10329.
[33] D. Das, K.K. Nanda, One-step, integrated fabrication of Co 2 P nanoparticles encapsulated N, P dual-doped CNTs for highly advanced total water splitting, Nano Energy 30 (2016) 303–311.
[34] Y. Yao, B. Zhang, J. Shi, Q. Yang, Preparation of nitrogen-doped carbon nanotubes with different morphologies from melamine-formaldehyde resin, ACS Appl. Mater. Interfaces 7 (2015) 7413–7420.
[35] L. Hu, R. Zhang, L. Wei, F. Zhang, Q. Chen, Synthesis of FeCo nanocrystals encapsulated in nitrogen-doped graphene layers for use as highly efficient catalysts for reduction reactions, Nanoscale 7 (2015) 450–454.
[36] N. Garino, A. Sacco, M. Castellino, J.A. Muñoztabares, A. Chiodoni, V. Agostino, V. Margaria, M. Gerosa, G. Massaglia, M. Quaglio, Microwave-assisted synthesis of reduced graphene oxide/SnO2 nanocomposite for oxygen reduction reaction in microbial fuel cells, ACS Appl. Mater. Interfaces 8 (2016) 4633–4643.
[37] S.H. Ahn, A. Manthiram, Self-templated synthesis of Co-and N-Doped carbon microtubes composed of hollow nanospheres and nanotubes for efficient oxygen reduction reaction, Small 13 (2017), 1603437.
[38] A.N. Popova, Y.A. Zaharov, V.M. Pugachev, Chemical synthesis, structure and magnetic properties of nanocrystalline Fe-Co alloys, Mater. Lett. 74 (2012) 173–175.
[39] J. Kim, B.L. Sang, K.L. Sang, K.H. Kim, Magnetic thermal dissipations of FeCo hollow fibers filled in composite sheets under alternating magnetic field, Appl. Surf. Sci. 415 (2016).
[40] J. Zhang, L. Qu, G. Shi, J. Liu, J. Chen, L. Dai, N, P-Codoped carbon networks as efficient metal-free bifunctional catalysts for oxygen reduction and hydrogen evolution reactions, Angew. Chem. 128 (2016) 2270–2274.
[41] M. Shao, Q. Chang, J.P. Dodelet, R. Chenitz, Recent advances in electrocatalysts for oxygen reduction reaction, Chem. Rev. 116 (2016) 3594.
[42] K. Gong, F. Du, Z. Xia, M. Durstock, L. Dai, Nitrogen-doped carbon nanotube arrays with high electrocatalytic activity for oxygen reduction, Science 323 (2009) 760–764.
[43] C. Zhang, B. An, L. Yang, B. Wu, W. Shi, Y.-C. Wang, L.-S. Long, C. Wang, W. Lin, Sulfur-doping achieves efficient oxygen reduction in pyrolyzed zeolitic imidazolate frameworks, J. Mater. Chem. A 4 (2016) 4457–4463.
[44] L.-L. Feng, G.-D. Li, Y. Liu, Y. Wu, H. Chen, Y. Wang, Y.-C. Zou, D. Wang, X. Zou, Carbon-armored Co9S8 nanoparticles as all-pH efficient and durable H2-evolving electrocatalysts, ACS Appl. Mater. Interfaces 7 (2015) 980–988.
[45] C. Domínguez, F.J. Pérez-Alonso, S.A. Al-Thabaiti, S.N. Basahel, A.Y. Obaid, A.O. Alyoubi, J.L.G.D.L. Fuente, S. Rojas, Effect of N and S co-doping of multi-walled carbon nanotubes for the oxygen reduction, Electrochim. Acta 157 (2015) 158–165.
[46] H. Zhu, J. Zhang, R. Yanzhang, M. Du, Q. Wang, G. Gao, J. Wu, G. Wu, M. Zhang, B. Liu, When cubic cobalt sulfide meets layered molybdenum disulfide: a core–shell system toward synergetic electrocatalytic water splitting, Adv. Mater. 27 (2015) 4752–4759.
[47] M.C. Biesinger, B.P. Payne, A.P. Grosvenor, L.W. Lau, A.R. Gerson, R.S.C. Smart, Resolving surface chemical states in XPS analysis of first row transition metals, oxides and hydroxides: Cr, Mn, Fe, Co and Ni, Appl. Surf. Sci. 257 (2011) 2717–2730.
[48] Y. Zhao, K. Kamiya, K. Hashimoto, S. Nakanishi, Efficient bifunctional Fe/C/N electrocatalysts for oxygen reduction and evolution reaction, J. Phys. Chem. C 119 (2015) 2583–2588.
[49] W. Niu, L. Li, X. Liu, N. Wang, J. Liu, W. Zhou, Z. Tang, S. Chen, Mesoporous N-doped carbons prepared with thermally removable nanoparticle templates: an efficient electrocatalyst for oxygen reduction reaction, J. Am. Chem. Soc. 137 (2015) 5555–5562.
[50] Y.J. Sa, D.-J. Seo, J. Woo, J.T. Lim, J.Y. Cheon, S.Y. Yang, J.M. Lee, D. Kang, T.J. Shin, H.S. Shin, A general approach to preferential formation of active Fe–N x sites in Fe–N/C electrocatalysts for efficient oxygen reduction reaction, J. Am. Chem. Soc. 138 (2016) 15046–15056.
[51] C.W.B. Bezerra, L. Zhang, K. Lee, H. Liu, A.L.B. Marques, E.P. Marques, H. Wang, J. Zhang, A review of Fe–N/C and Co–N/C catalysts for the oxygen reduction reaction, Electrochim. Acta 53 (2008) 4937–4951.
[52] D. Malko, A. Kucernak, T. Lopes, In situ electrochemical quantification of active sites in Fe–N/C non-precious metal catalysts, Nat. Commun. 7 (2016).
[53] S.H. Noh, H.S. Min, J. Kang, T. Okajima, B. Han, T. Ohsaka, Towards a comprehensive understanding of FeCo coated with N-doped carbon as a stable bi-functional catalyst in acidic media, NPG Asia Mater. 8 (2016) e312.